JACS
JOURNAL OF THE AMERICAN CHEMICAL SOCIETY

Article

pubs.acs.org/JACS

Hydrogen-Incorporated TiS_2 Ultrathin Nanosheets with Ultrahigh Conductivity for Stamp-Transferrable Electrodes

Chenwen Lin,[†,§] Xiaojiao Zhu,[†,§] Jun Feng,[†] Changzheng Wu,*[,†] Shuanglin Hu,[‡] Jing Peng,[†] Yuqiao Guo,[†] Lele Peng,[†] Jiyin Zhao,[†] Jianliu Huang,[†] Jinlong Yang,[†] and Yi Xie*[,†]

[†]Division of Nanomaterials and Nanochemistry, Hefei National Laboratory for Physical Sciences at the Microscale, University of Science & Technology of China, Hefei, Anhui, 230026, P. R. China

[‡]Department of Materials Chemistry, the Ångström Laboratory, Uppsala University, Uppsala, Sweden, Box 538, S-75121

Supporting Information

ABSTRACT: As a conceptually new class of two-dimensional (2D) materials, the ultrathin nanosheets as inorganic graphene analogues (IGAs) play an increasingly vital role in the new-generation electronics. However, the relatively low electrical conductivity of inorganic ultrathin nanosheets in current stage significantly hampered their conducting electrode applications in constructing nanodevices. We developed the unprecedentedly high electrical conductivity in inorganic ultrathin nanosheets. The hydric titanium disulfide (HTS) ultrathin nanosheets, as a new IGAs, exhibit the exclusively high electrical conductivity of 6.76×10^4 S/m at room temperature, which is superior to indium tin oxide (1.9×10^4 S/m), recording the best value in the solution assembled 2D thin films of both graphene (5.5×10^4 S/m) and inorganic graphene analogues (5.0×10^2 S/m). The modified hydrogen on S−Ti−S layers contributes additional electrons to the TiS_2 layered frameworks, rendering the controllable electrical conductivity as well as the electron concentrations. Together with synergic advantages of the excellent mechanical flexibility, high stability, and stamp-transferrable properties, the HTS thin films show promising capability for being the next generation conducting electrode material in the nanodevice fields.

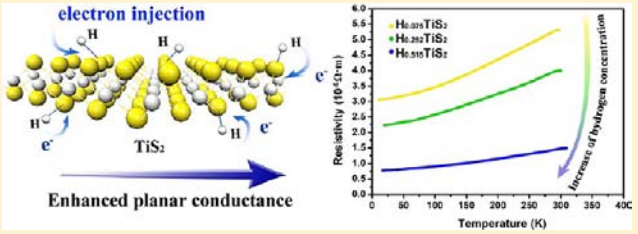

INTRODUCTION

Recently, ultrathin nanosheets of two-dimensional (2D) materials, such as graphene and inorganic graphene analogues (IGAs), have attracted tremendous attentions for their microscopic compressibility and macroscopic extensibility, benefiting their incorporations into nanoelectronic devices and flexible energy storage devices with ultrathinness.[1,2] Great efforts have been carried out to obtain these 2D materials with good conductive for high quality and transferrable thin electrodes, including solid-state and solution-based processes.[3−7] Although the growth of single-crystal monolayer and multilayer graphene domains by high-temperature solid-state reaction method successfully accomplished the remarkably high conductivity with the size scale ranging from the nanometer to submillimeter catering for the flexible nanoelectronic devices,[8,9] the 2D thin films of ultrathin nanosheets assembled from the solution-based strategies bring advantages of sufficient active materials, more flexible structural parameters, and the arbitrary film sizes with dimensional diversities. The solution assembled graphene films has received considerable attentions as thin electrodes for constructing diversified devices, such as supercapacitors and optoelectronics for their extreme flexibilities and in-plane conductivities.[10−14] Progresses have been achieved to upgrade the electrical performance by solution-based assembly methodologies, from vacuum-filtration assembled graphene film (~7.75×10^3 S/m),[3] Langmuir−Blodgett method assembled graphene film (4.17×10^4 S/m),[4] to dip coating assembled graphene film (5.5×10^4 S/m).[15] However, as another conceptually new class of 2D materials, IGAs' applications in flexible and high-conductive electrodes are still limited. Considering their characteristics of richer electronic structures and electron−electron correlations arising from the involved inorganic ingredients, IGAs provide a promising platform to develop the high in-plane conductance aside from graphene, which would bring out new fascinating alternatives that can be competitive with and even superior to the graphene. Moreover, sheets of inorganic atoms bonded in the rigid inorganic lattice frameworks of the IGAs bring higher mechanical strength and more stable electrical behavior with attractive applications in next-generation flexible nanodevices. Nevertheless, the obtainment of highly conductive IGAs materials remain elusive to date, in that most familiar IGAs are either semiconducting (MoS_2 and WS_2)[16] or insulating (BN and BCN).[17] Since the materials with metallic behavior most probably possess the capability of high conductivity, the exploration of metallic IGAs is quite urgent, in that rare researches about metallic IGAs were reported in the past few years.[5] The conductive IGA with metallic behavior in vanadium disulfide (VS_2) has shown relatively high conductivity ($5.0 \times$

Received: January 3, 2013
Published: March 8, 2013

   dx.doi.org/10.1021/ja400041f | J. Am. Chem. Soc. 2013, 135, 5144−5151

10^2 S/m),[5,18] and indeed there is still a long way to go since it is far lower than that of the assembled graphene film and the conventional electrode ITO. In addition, the highly chemical sensitivity of VS_2 hampers the embodiments of its intrinsic conductivity due to demolishing the conductive structures during the transferring process. Therefore, the pursuing of high-conductive ultrathin nanosheets for the assembly of IGA films is a long-term objective for researchers, which is challenging but noteworthy.

Theoretical work gave us the inspiration that titanium disulfide (TiS_2) would be a new catalogue of the high-conductive materials with graphene analogue structure. As a prototype of layered transition-metal dichalcogenides (TMDs), CdI_2-type titanium disulfide is composed of metal Ti layer sandwiched between two S layers forming edge-sharing TiS_6 octahedra with strong covalent bonding in plane.[19] Whereas, the adjacent S−Ti−S layers are coupled to each other by weak van der Waals interactions, providing the practical feasibility for exfoliating the bulk TiS_2 to ultrathin nanosheets of TiS_2.[20−23] As is known, with the variation of the carrier concentration triggered by exotic electrons injections into the inorganic lattice frameworks,[24] the reinforcement of the electron−electron correlations of infinite S−Ti−S framework would be induced, resulting in the consequent improvement of conductivity in the 2D system. Furthermore, the only two valence states of Ti in the simple inorganic system, i.e., Ti^{3+} and Ti^{4+}, ensures the stabilization of the S−Ti−S framework without structural destructions when the extra electrons injected, benefiting both high conductivity and stability in TiS_2. Therefore, controlling the electronic behavior in layered TiS_2 structure provides the promising signs to achieve a highly conductive new graphene analogue.

However, although the TiS_2 lattice framework shows the prospective signs in unique electrical properties, the in-depth investigation has been significantly neglected for precisely regulating the electronic structure of TiS_2 IGA and even integration into the thin flexible devices. Herein, we highlight an efficiently chemical exfoliation way to achieve metallic hydric TiS_2 (HTS) ultrathin nanosheets, as a new IGAs, in which the incorporation of hydrogen can be tuned with different concentrations. The modified hydrogen on each TiS_2 monolayer donates the extra electrons into the S−Ti−S layers to enhance the electron−electron correlations in the 2D lattice framework, thus leading to the great conductivity enhancement with the hydrogen involved. The assembly of HTS nanosheets into tightly thin films behaves an excellent electrical conductivity 6.76×10^4 S/m at 298 K, which is superior to indium tin oxide (ITO, 1.9×10^4 S/m),[25] representing the best value among the solution assembled thin films of the graphene (5.5×10^4 S/m) and inorganic graphene analogues (5.0×10^2 S/m). Moreover, with the addition of the synergic advantage of mechanical and stamp-transferrable properties, we demonstrate the great potential of HTS film for flexible and transferrable thin conducting electrode in the nanodevice fields.

EXPERIMENTAL SECTION

Materials. Titanium powder (99.9%) was commercially available from Aladdin Chemical Co. Ltd. Sulfur powder, iodine (analytical grade), and *n*-butyl-lithium (*n*-BuLi) (2.5 M in hexane) were purchased from Sinopharm Chemical Reagent Co. Ltd. Bulk TiS_2 was prepared according to literature.[26]

Exfoliation of the Precursor Li_xTiS_2 into Hydric TiS_2 Ultrathin Nanosheets. The 10 mg as-prepared Li_xTiS_2 was dispersed in 20 mL distilled water. Then the solution was bubbled with nitrogen to expel the dissolved oxygen molecules for avoiding the oxidation. The above Li_xTiS_2-included dispersion was immersed into the ice water and ultrasonicated for 1 h. Afterward, the resultant modena suspension was centrifuged at 2500 rpm for 20 min. Then the supernatant was decanted into another container to remove the unexfoliated flakes, and a high-quality dispersion of hydric TiS_2 nanosheets was obtained.

Preparation of Precursor Li_xTiS_2. In a typical procedure, the Li_xTiS_2 was synthesized by the lithium intercalation using 15 mg TiS_2 powder with 0.5 mL *n*-BuLi diluted by 4 mL hexane in a customized glass vacuum system reacted at 60 °C and stirred for gradient time 3, 6, and 12 h to obtain the Li-intercalated TiS_2 with gradient increases of lithium concentration. The resultant dispersions were in dark brown and filtered, washed with cyclohexane and anhydrous ethanol for several times, and then vacuum dried at 60 °C for the following experimental procedures.

Assembly of Hydric TiS_2 Nanosheets into Transferrable Thin Films. Hydric TiS_2 nanosheets solution was vacuum filtrated over a cellulose membrane with 0.22 μm pore size to form a homogeneous thin film, of which the thickness can be changed by the filtrated amount of HTS nanosheet solution. The films we used for the testing were always controlled to be ∼400 nm which could be identified by the scanning electron microscopy (SEM, Figure S7).

Dry-Transferring of Hydric TiS_2 Thin Film to Arbitrary Substrates. The typical transferring procedure includes the following steps: (1) Forming the hydric TiS_2 thin film: the as-obtained HTS nanosheet dispersions were vacuum filtrated onto the cellulose membrane forming a homogeneous hydric TiS_2 film; and (2) using PDMS as intermediate transferring stamp: the PDMS stamp was attached to the hydric TiS_2 film with the manual squeeze pressure for ∼5 min, and then the hydric TiS_2 thin film could be lifted up by the PDMS stamp, leaving the adhered film to the bottom area of the PDMS stamp. When the PDMS stamp is contacted to the target substrate, such as PET, silicon wafer, metal surface, and then hydric TiS_2 film could be transferred to the arbitrary target substrate.

Characterizations. X-ray diffraction (XRD) were performed on a Philips X'Pert Pro Super diffractometer with Cu K_α radiation (λ = 1.54178 Å). The transmission electron microscopy (TEM) images were obtained on a JEOL-2010 transmission electron microscope at an acceleration voltage of 200 kV. The field emission scanning electron microscopy (FE-SEM) images were taken on a JEOL JSM-6700F SEM. HR-TEM images were taken on a JEOL 2010 microscope at an accelerating voltage of 200 kV. Scanning transmission electron microscopy (STEM) images, energy dispersive X-ray spectra (EDS) and electron energy lost spectra (EELS) were obtained on a JEM 2100F (field emission) transmission electron microscopes equipped with an Oxford INCA x-sight EDS Si(Li) detector at an acceleration voltage of 200 kV. ^{1}H solid-state MAS NMR spectra were obtained with a 500.132 MHz NMR spectrometer (Bruker, Germany) at 298 K. X-ray photoelectron spectra (XPS) were acquired on an ESCALAB MK II with Mg K_α as the excitation source. The electrical transport property measurements were carried out using a Keithley 4200-SCS Semiconductor Characterization System and a four-point probe method. Hall coefficient and magnetoresistance were measured by a four-probe technique using a Quantum Design Physical Property Measurement System (PPMS)-9 using the van der Pauw method. Electrochemical station (CHI 660B) was used for measurements of the electrical endurance properties. Gold contacts were evaporated over the sample through a stencil mask, and copper wires were embedded and connected to gold contacts with silver paste as the leads, which enables a strong electrical contact and consequently a small contact resistance. The scanning conductance microscopy (SCM) with interleave mode of our AFM [Digital Instrument Nanoscope V] was utilized to investigate the intrinsic nanoelectronic property of the nanosheets. The infrared spectra were measured on a NICOLET Fourier transform infrared spectrometer, using pressed KBr tablets. Raman spectra were recorded at room temperature with a LABRAM-HR Confocal Laser Micro Raman Spectrometer 750 K with a laser power of 0.5 mW.

dx.doi.org/10.1021/ja400041f | J. Am. Chem. Soc. 2013, 135, 5144−5151

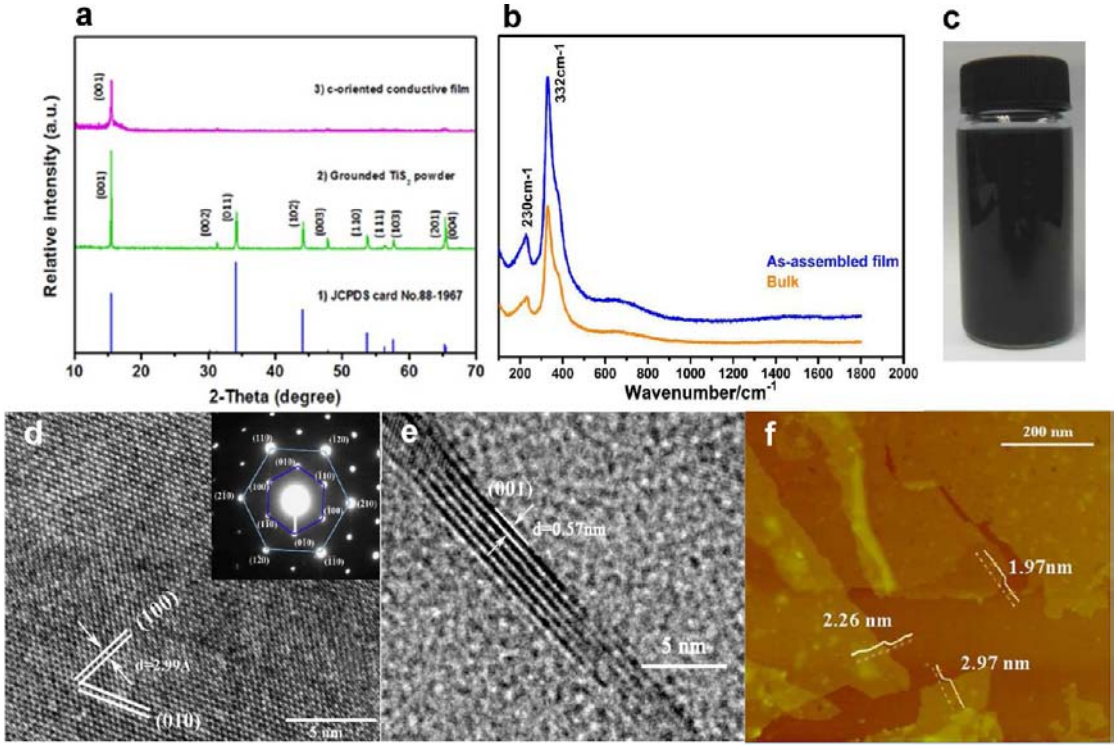

Figure 1. Ultrathin hydric titanium disulfide graphene analogue. (a) XRD pattern of the as-assembled HTS film with highly *c*-orientation, confirming the 1T-TiS_2 structure and the highly *c*-axis orientations; (b) Raman spectra of bulk TiS_2 and as-assembled film; (c) homogeneously dispersed HTS nanosheets suspension; (d,e), HR-TEM and SA-ED analyses of the obtained TiS_2 nanosheets; and (f) tapping mode AFM image of the exfoliated TiS_2 nanosheets.

RESULTS AND DISCUSSION

The atomic-thin HTS nanosheets was obtained by the exfoliation of intermediate precursor Li-intercalated TiS_2 (Li_xTiS_2) through a forced hydrogen incorporation process during the exfoliating process.[27,28] In such process, the incorporated lithium ions in the Li_xTiS_2 play the important role in the efficient exfoliation, which would expand the interlayer distance, and thus weaken the van der Waals interactions between the layers. And the following hydrolysis reaction as well as one hour of ultrasonic treatment assisted the breaking of the weak interlayer van der Waals interactions, resulting in the atomic-thin hydrogen incorporated TiS_2 nanosheets. Gradient hydrogen contents of HTS nanosheets retaining the 1T-TiS_2 lattice framework were selectively controlled by the different lithiation time of 3, 6, and 12 h, and these three samples can be denoted as $H_{0.075}TiS_2$, $H_{0.292}TiS_2$, and $H_{0.515}TiS_2$. The systematical characterizations verified the incorporation of hydrogen atoms and the 1T S−Ti−S lattice framework was maintained, forming the 1T hydric TiS_2. The structural information of the samples could be revealed by the XRD, Raman spectra, and HRTEM. The XRD patterns provide direct phase information for the HTS nanosheets. The XRD pattern of the raw material could be readily assigned to the 1T-TiS_2 as shown in the middle curve of Figure 1a, which is in accordance with the standard JCPDS card no. 88-1967 (TiS_2, space group $P\bar{3}m1$, a = 3.4073 Å, c = 5.6953 Å). After the exfoliation of the TiS_2 raw material, as a consequence of microscopic self-orientation of quasi-2D HTS ultrathin nanosheets, the assembled thin film transferred onto the silicon wafer also exhibits the highly *c*-axis orientation, as is revealed by the pattern shown in the up curve of Figure 1a, in that only one diffraction peak of (001) facet could be obviously observed. The highly orientation along the [001] direction represents the high quality of the assembled quasi-2D nanosheets film with the crystal form of 1T TiS_2. The Raman spectra (Figure 1b) further confirm that there are no structural changes of 1T-TiS_2 before and after the exfoliation due to the particularly sensitive to the microstructure of inorganic crystal structure for the Raman methods. The Raman spectra of the bulk TiS_2 and final HTS product show the 230 and 332 cm^{-1} and the a shoulder at about 380 cm^{-1} (Figure 1b), which map exactly onto a reported literature spectrum of TiS_2.[29] In a word, the structural comparison between the bulk TiS_2 and the HTS gives the common 1T-TiS_2 polymorph, although the hydrogen was incorporated.

HRTEM investigation (Figure 1d,e) reveals the microscopic phase information as well as the thickness of the HTS graphene analogue. The HRTEM images and its corresponding SAEDs were performed on a typical ultrathin nanosheet as shown in Figure 1d. The interplanar distance of 2.99 Å matched well with the plane distances of d_{100} and d_{010}, respectively, of the facets of TiS_2 (2.950 Å). The orientation angle values 60° of these two planes of (100) and (010) appeared in the SAED patterns, and the lattice fringes in HRTEM image were fairly consistent with those calculated from hexagonal crystallographic parameters of 1T-TiS_2. Energy-dispersive X-ray spectroscopy, the EELS and elemental mapping (Figure S5) confirm the product has the chemical formula of TiS_2, and no other obvious contaminants can be found in the as-obtained products. (Note that hydrogen atoms were invisible for these kinds of characterization methods). HRTEM image performed on one typical cross-section edge of the ultrathin nanosheet structures (Figure 1e), indicating an interlayer spacing of ~0.57 nm for (001) plane. Moreover, as is presented in Figure 1e, five to six dark and

dx.doi.org/10.1021/ja400041f | J. Am. Chem. Soc. 2013, 135, 5144−5151

bright lattice fringes can be readily identified, indicating that the sample was stacked up with five to six single layers, which could be further verified by the following AFM results. As illustrated in Figure 1f, tapping mode AFM was performed to further evaluate the thickness of the as-prepared HTS nanosheets. And the measured heights of the nanosheet regions were 1.97 and 2.97 nm, corresponding to 3 and 5 layers, respectively, in that the *c* parameter of TiS_2 is 5.70 Å. These characterization results clearly demonstrated that the raw bulk TiS_2 was successfully exfoliated into the ultrathin nanosheets with good quasi-2D crystallinity, providing the necessary prerequisite for the assembly into large-area practical devices.

Elemental ingredients especially for the involving of hydrogen element of the H_yTiS_2 could be revealed by the Fourier transform infrared spectroscopy (FT-IR), ^1H solid-state MAS NMR spectra (Figure S8) and XPS analyses. Characteristic absorption peaks (ν_{S-H}: 2515 cm^{-1}) in FT-IR spectra validate the formation of S−H bonding in the HTS structure, and signals at 3.04 ppm in the ^1H solid-state MAS NMR spectra confirm the hydrogen atoms are solely bonded to the S atoms in the form of H−S bonds. As described above, in spite of the hydrogen incorporation in the TiS_2 structure, the S−Ti−S lattice framework was maintained, and no obvious structural changes can be observed, verifying our structural model of the H_yTiS_2 with the hydrogen atoms modifying on the S−Ti−S layers. Moreover, the auxiliary evidence of the presence of H_yTiS_2 comes from the careful analysis of XPS results, in that the incorporation of hydrogen in the meantime leads to the different concentrations of Ti^{4+} and Ti^{3+} that can be unraveled by the XPS spectrum. The Ti 2p region in the XPS spectra of the samples prepared from Li_xTiS_2 of different lithiation times, i.e., 3, 6, and 12 h, was shown in Figure 2a. The Ti 2p spectra consist of quadruple peaks, suggesting the mixed titanium valence states. Furthermore, additional peaks that appear at 462.1 and 456.1 eV are found besides the known doublet peaks of Ti^{4+} $2p_{1/2}$ (464.5 eV) and Ti^{4+} $2p_{3/2}$ (458.8 eV),[30] which are ascribed to the Ti^{3+} $2p_{1/2}$ and Ti^{3+} $2p_{3/2}$.[31] After the Shirley background subtraction, the Ti 2p peaks were deconvoluted to show the Ti^{4+} and Ti^{3+} contributions. The concentration ratios of Ti^{4+}/Ti^{3+} in the Li_xTiS_2 samples with 3, 6, and 12 h lithiation time are calculated to be 12.293, 2.420, and 0.943, respectively. In our case, the total valence of the product by the appearance of Ti^{3+} has been found to be compensated by the incorporation of hydrogen atoms. Since the hydrogen atoms were invisible for many kinds of characterization methods and the precisely quantitative determination of our HTS product still has the practical difficulty, the amounts of Ti^{3+} give the vital clue to conclude the molecular formula as $H_{0.075}TiS_2$, $H_{0.292}TiS_2$ and $H_{0.515}TiS_2$. The Ti^{3+} 2p peaks exhibit a distinct and consecutive increase in the bottom to top curves verifying the correlatively increasing of hydrogen concentration when the lithiation time of the intermediate product varied from 3, 6, to 12 h, with which the tunable hydrogen incorporation in the HTS nanosheets was successfully obtained.

The incorporation of hydrogen atoms to the 1T TiS_2 originates from its unique structural features. The titanium element has only two valence states of Ti^{3+} and Ti^{4+} in the simple system, which facilitates Ti^{4+} to be targetedly reduced into Ti^{3+} in the reducing reaction process with a very simple electron transferring process. And in fact the only two valence states of Ti ensures the stabilization of the S−Ti−S framework without structural destructions when the extra hydrogen incorporations. In our case, the H_yTiS_2 graphene analogues

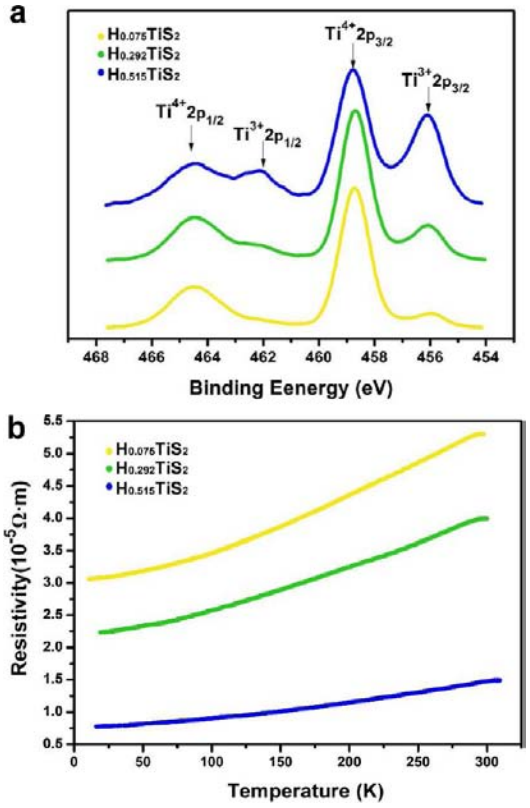

Figure 2. Hydrogen incorporation endowing the excellent electrical conductivity. (a) XPS of Ti 2p core level peak regions for different samples, revealing the increasing concentration ratios of Ti^{3+} and Ti^{4+} as the lithiation reaction time elongated; and (b) temperature-dependent electrical resistivity for samples shown in (a), showing the successful regulation of conductivity through controlling hydrogen concentration.

were formed by two steps: (1) the formation of Li_xTiS_2 by the insertion and reduction of bulk TiS_2 by *n*-butyl lithium in the *n*-hexane solution; and (2) following hydrolysis process of the Li_xTiS_2 to form the final H_yTiS_2 graphene analogues in the ultrasound process. The former step determines the reduction degree from Ti^{4+} to Ti^{3+}, which answers for the H-incorporation amounts in the final HTS product. The latter step is the hydrolysis of Li_xTiS_2 to form the final H_yTiS_2 with the reaction equation of $Li_xTiS_2 + H_2O \rightarrow H_yTiS_2 + LiOH$, in which higher value of Li content in Li_xTiS_2 results in the increase of *y* value in H_yTiS_2. As expected, the involved different amounts of hydrogen atoms strongly relied on the lithiation reaction time, and the lithiation reaction time of 3, 6, and 12 h resulted in the $H_{0.075}TiS_2$, $H_{0.292}TiS_2$, and $H_{0.515}TiS_2$, respectively. With such process, the hydrogen contents could be controlled based on the 1T-TiS_2 structure. In the formation process of H_yTiS_2, the redox reaction forming the nonuniform electron distribution in the S−Ti−S framework provides the suitable sites for hydrogen modification. As a consequence, the hydrogen atoms were demonstrated to bond to S atoms on the S−Ti−S plane forming the stability of S−Ti−S framework.

Hydric S−Ti−S framework in H_yTiS_2 provides the feasibility to introduce exotic electrons into infinite S−Ti−S framework, which would effectively regulate the electrical property of the as-prepared HTS samples. To study the influence of electron doping on the electrical conductivity, the transport properties of the corresponding assembled H_yTiS_2 thin films with a

dx.doi.org/10.1021/ja400041f | J. Am. Chem. Soc. 2013, 135, 5144−5151

gradual increasing of hydrogen contents of $H_{0.075}TiS_2$, $H_{0.292}TiS_2$, and $H_{0.515}TiS_2$ were examined. As is shown in Figure 2b, the temperature-dependent electrical resistivity (ρ) of all the three HTS samples was quite lower than that of the synthetic bulk TiS_2 with ~1.91×10^{-4} Ω·m at 298 K (Figure S6), and they showed the decrease of electrical resistivity as the temperature decreased with $d\rho/dT > 0$, behaving the metallic character. Moreover, as shown in Figure 2b, the obvious enhancement of the electrical conductivity occurs with the increasing hydrogen concentrations from $H_{0.075}TiS_2$, $H_{0.292}TiS_2$, to $H_{0.515}TiS_2$ films. In this case, the assembled $H_{0.515}TiS_2$ film with highest hydrogen concentration accomplished the lowest resistivity of 7.79×10^{-6} Ω·m at 20 K and 1.48×10^{-5} Ω·m at the room temperature. Of note, the assembly of HTS nanosheets into tightly thin films behaves an excellent electrical conductivity 6.76×10^4 S/m at 298 K, recording the best value in the solution assembled 2D thin films of both graphene (5.5×10^4 S/m) and inorganic graphene analogues (5.0×10^2 S/m), even superior to ITO (1.9×10^4 S/m) reported so far.

To inspect the microscopic conductive properties of the yielded HTS nanosheets, SCM was utilized to image the conductivity of the HTS nanosheets with the interleave mode of AFM.[32−35] In our case, the sample dispersion of HTS nanosheets for SCM analysis is prepared without centrifugation to provide different thicknesses of nanosheets for the sake of comparison. The selected two pieces of nanosheets labeled as sheets 1 and 2 (8.91 and 4.49 nm, respectively) were shown in SCM image (Figure 3a) with difference of depth in color, which was as a result of the difference phase shifts ($\Delta\varphi$) of the two nanosheets (Figure 3c). Notably, the thicknesses of both nanosheets were given by AFM analysis as shown in the inset of Figure 3a. The process for obtaining data above was involved with a dual-pass imaging pass operation. In the first pass, the ac mode image mapping was used to obtain a topography profile. In the second pass, the tip was lifted up to 20 nm high above the topographical baseline. A 4 V DC voltage (V_{tip}) was applied between the conductive tip and the SiO_2/p-type Si substrate, as shown in Figure 3b. The variation of phase shift values between sheets 1 and 2 arose from the different film thickness which can be understood by considering the cantilever tip, nanosheet, and the degenerately doped Si as capacitor elements.[32,35] The voltage applied between the tip and the substrate produces electrostatic forces on the tip that alter f_0 (the cantilever's resonant frequency) and φ (phase).When the tip is over the conductive nanosheet, the tip-induced charge modulation within the nanosheet produces additional electrostatic tip−sample forces. In this case, the magnitude of these forces, and hence φ are determined by the electric field between the tip-sheet and the sheet-ground-plane capacitors. As known, the weak van der Waals interactions in the layered compound hindering the electrons transportation in c axis increase the capacitance of the sheets. Therefore, thinner nanosheet has less capacitance to the ground plane compared with the thicker one, and their potential floats nearer to the applied voltage, yielding smaller tip−sample voltage and smaller phase shifts. Moreover, the phase shift ($\Delta\varphi$) of both of the nanosheets regions with respect to the bare SiO_2 substrate were negative, which showed conductive characteristic, and were similar to metallic graphene,[35] confirming the high conductance of HTS nanosheets from a microscopic evidence viewpoint.

Perdew−Burke−Ernzerhof (PBE) exchange−correlation functional and density functional theory calculations with consideration of the on-site Hubbard U (DFT+U) on the

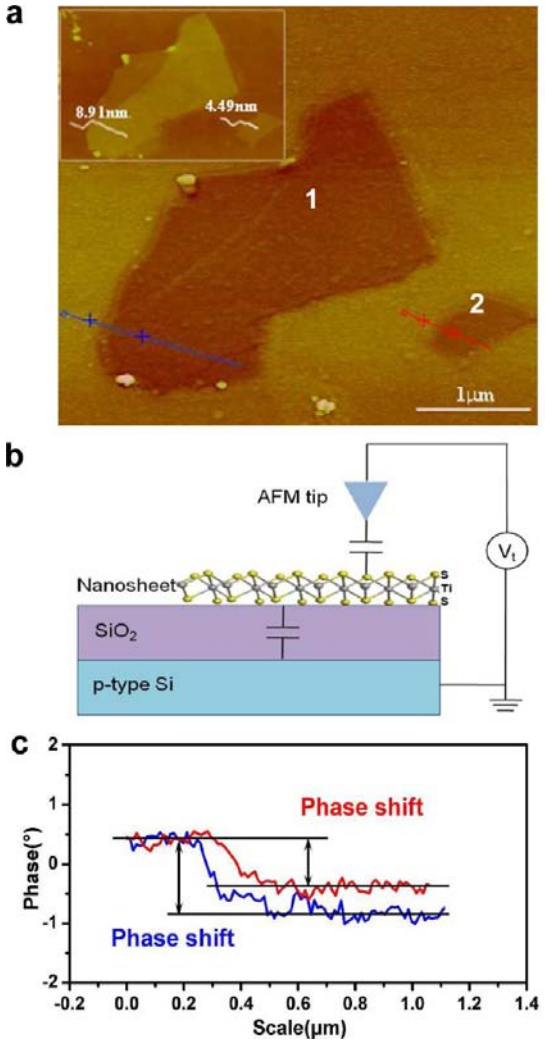

Figure 3. Microscopic conductance explored by SCM. (a) Scanning conductance image for the exfoliated nanosheet; (b) schematic illustration of SCM upon the HTS graphene analogues; and (c) corresponding line profiles along the blue and red line as shown in (a).

electronic properties of electron-injected TiS_2 provide further help to the understanding of the nature of conductivity regulation. Revealed by the calculation results, hydrogen revealed by the calculation results, hydrogen incorporation indeed greatly enhanced the conductivity of HTS nanosheets. In detail, the electron doping model was adopted to simulate different concentrations of electrons in monolayer TiS_2, with the doping concentration corresponds to 1, 1/4, 1/9, and 1/16 of 9.51×10^{14} cm^{-2}, respectively. According to the PBE theoretical investigations, the monolayer of TiS_2 is a semimetal (Figure S1). After doping electrons, the monolayer of TiS_2 became metal, the density of states (DOS) of the one electron doping to unit cell and a $4 \times 4 \times 1$ supercell system is compared in Figure 4a. The doped electrons increased the electron concentration in the conduction band, which indicates larger conductivity of more reduced system. The electrical resistance was also calculated directly from the eigen values in each doped system showing a negative correlation with electron concentration, as shown in Figure 4b. The theoretical electrical resistance is ~10^{-5} Ω·m, within the experimental results, consolidating the successful conductivity enhancement by hydrogen incorporation in the HTS nanosheets.

dx.doi.org/10.1021/ja400041f | J. Am. Chem. Soc. 2013, 135, 5144−5151

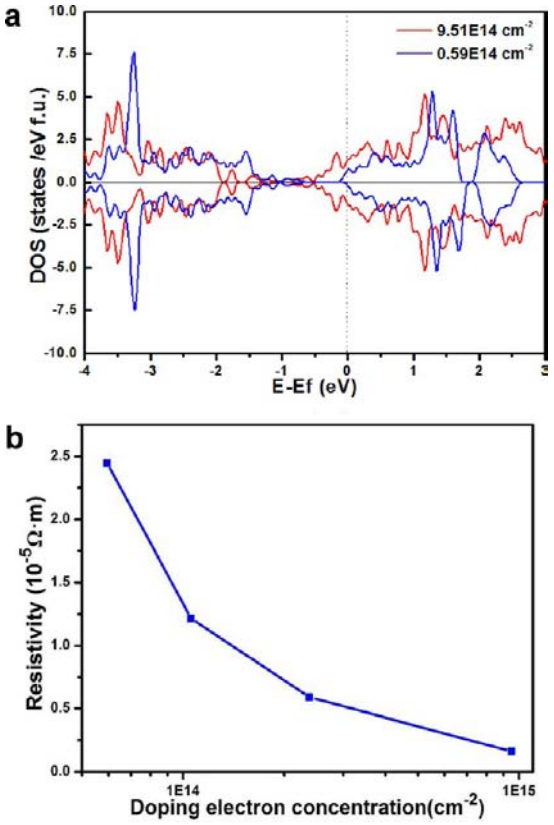

Figure 4. Theoretical calculations unraveling the nature of ultrahigh electrical conductivity. (a) Comparison of the DOS of pure TiS_2 monolayer with the doped electron concentration of 9.51×10^{14} and 0.59×10^{14} cm^{-2} in TiS_2, calculated by DFT+U (f.u. stands for formula unit). (b) The simulated electrical resistance varying with applied doping electron concentrations.

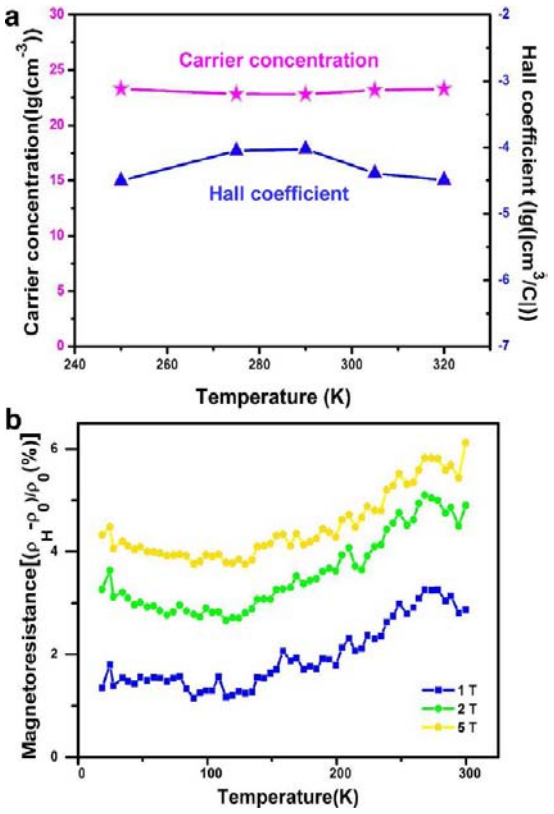

Figure 5. Unique metallic behavior of the as-assembled hydric titanium disulfide film. (a) Temperature-dependent on Carrier concentration and Hall coefficient of the as-assembled HTS film; and (b) temperature-dependent on the magnetoresistance under different magnetic fields 1, 2, and 5 T.

The Hall coefficient (R_H) measurements and the magnetoresistance (MR) curve were performed to further understand the charge transport properties in the as-assembled HTS film, taking the $H_{0.515}TiS_2$ assembled film as a typical example. As is illustrated in Figure 5a, the Hall coefficients (R_H) under different temperatures were all negative, indicating the carriers are electrons. The carrier concentrations calculated from Hall coefficient (R_H) showed no obvious change with the increasing temperature. Of note, the electron concentration ($\sim 2 \times 10^{23}$ cm^{-3}) is 3 orders of magnitude larger than that in the bulk titanium disulfide,[26] thus verifying that the hydrogen incorporation structure in the as-assembled thin film leading to the feasibility of high conductivity performance. The MR, which demonstrates the resistivity changes after the magnetic field was applied, was also measured under a series of different magnetic fields. In our case, the as-assembled film displayed the positive MR under different magnetic fields 1, 2, and 5 T. As is known, when applied to magnetic fields, the motion path of electrons changes with Lorentz force, which results in the increasing possibility of electron−lattice scattering, thus leading to the increase of resistivity. As shown in Figure 5b, MR, defined as $(\rho_H - \rho_0)/\rho_0$, achieved 6% at 5 T (the topmost plot) where ρ_H and ρ_0 stand for resistivity under magnetic fields and the primitive resistivity, respectively. Of note, metals usually exhibit ordinary MR which is within 10% positive MR,[36] consolidating the metallicity of HTS nanosheets. All these results above confirm the HTS film to be a metallic high-conductive film, thereby showing the promising application as conductive thin electrode.

Assembly of ultrathin conductive nanosheets into large-area thin films is an essential process for developing the materials into practical electrical nanodevice applications. Due to the strong cohesive forces within the film arising from the van der Waals interactions,[3] the as-obtained film shows high quality with tightly compressed layer-by-layer structure (Figure S7). And thus the as-assembled HTS film exhibits the excellent properties of high voltage withstanding and mechanical stability, which endow it with the promising applications as conductive thin electrodes. As illustrated in Figure 6a, the as-assembled HTS film transferred onto the glass substrate with the length of 7 mm and width of 2 mm showed very good electrical endurance when applied 10 V for 4800 s in the ambient atmosphere, verifying its remarkably great stability over high voltage and long electrically applied time. Afterward, the aforementioned film were connected in series to 19 blue light-emitting diodes (LED) with a 3.2 V lowest working potential, as shown in Figure 6b,c. Apparently, the tandem unit worked well where the film played the role of electrical wire. Furthermore, when severely crumpled, the film transferred onto the PET still worked well (Figure S9), showing its perfect mechanical endurance. Combined the high conductivity and the remarkably great stability upon the electrical current applied, the HTS film behaves both the high mechanical endurance and the excellent electrical properties which are vital for the construction of future-generation nanodevices as the thin-film electrodes.

dx.doi.org/10.1021/ja400041f | J. Am. Chem. Soc. 2013, 135, 5144−5151

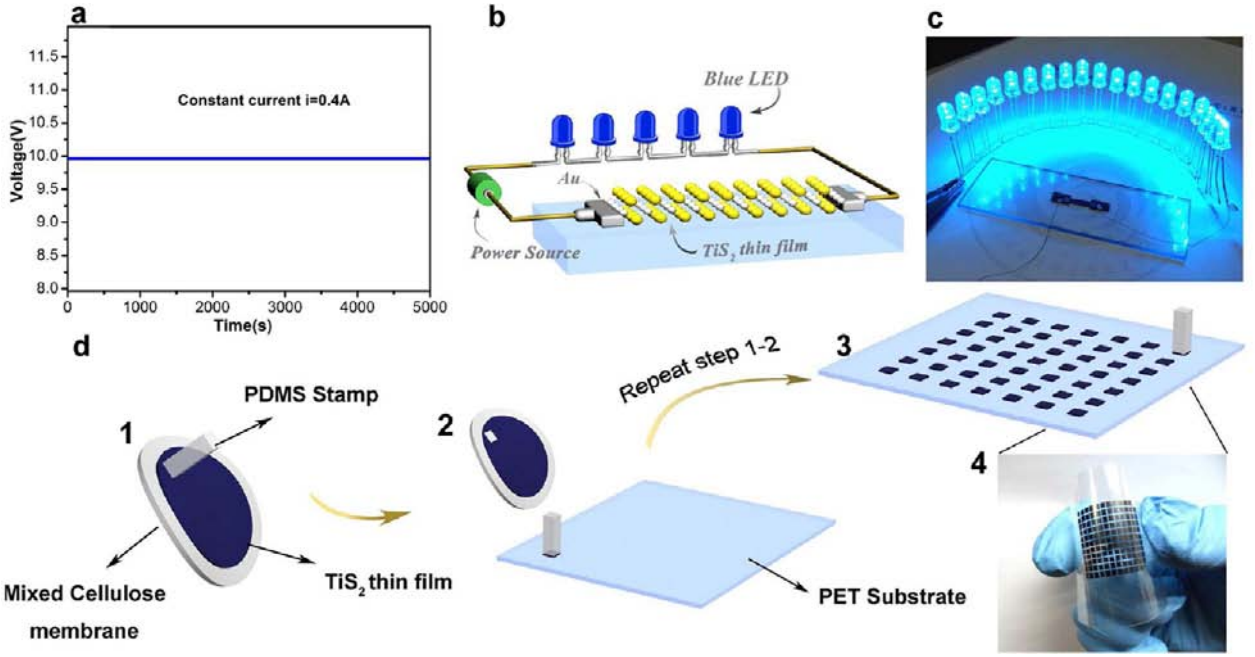

Figure 6. Excellent high-voltage endurance and improved dry-transfer method for transferrable assembled HTS film. (a) Time-dependent voltage value curve showing the high-voltage endurance with high stability. (b) Schematic illustration of working model for endurance test. (c) Digital photograph of the stability testing setup. (d) Schematic illustration of transfer-printing procedure (1−2) and the designed patterns (3−4).

Moreover, for the macroscopic electrode applications, an improved dry-transfer technique was developed based on polydimethysiloxane (PDMS) stamp which was formerly employed to obtain large-scale graphene films.[6] In our work, the as-assembled film can be readily transferred to any substrate, i.e., polyethylene terephthalate (PET), glass, polymethyl-methacrylate (PMMA), and silicon wafer (Figure S10). Briefly, to start the transfer, the PDMS stamp was contacted with the HTS film onto the receiving substrate and then suppressed with an appropriate pressure, at last the adhered film on the PDMS was transferred onto the receiving substrate by simply removing the PDMS. The transfer process is highly efficient, which is ascribed to the aforementioned cohesive forces between the HTS sheets and the substrate.[3] By using different shapes of PDMS, various shapes of HTS films can be transferred to arbitrary substrate. Based on the technique, a 10 × 10 matrix pattern was designed as shown in Figure 6d. This dry-transfer technique turns out to be very useful in making large-area thin electrodes without the lithography technique or the milder heating procedure in transferring process.[37] This convenient availability of the high-conductive film and safe transfer to the target substrate without intense mechanical or chemical treatments prohibits the conductive structure from being demolished, thus ensuring the high conductivity performance maintained. On the whole, the stamp-transferrable property, together with its high conductivity and remarkably great stability of the HTS film has seen the advances for an excellent electrode material that could be incorporated in various nanodevices.

■ CONCLUSION

In conclusion, we successfully obtained new hydric titanium disulfide (HTS) graphene-like ultrathin nanosheets, with less than five atomic layers, by an efficiently chemical exfoliation method, of which the electrical conductivity can be greatly enhanced by hydrogen incorporation. The hydric titanium disulfide realized an unprecedentedly high electrical conductivity in the assembled thin films behaving the conductivity as high as 6.76×10^4 S/m at 298 K, which is the best value reported among the solution assembled thin films of graphene and graphene analogues and even superior to conventional conducting ITO. Together with synergic advantages of the excellent mechanical flexibility, remarkably great stability, and ready stamp-transfer to any substrates, our HTS thin films show promising capability for being the next generation electrode material in the nanodevice fields. We anticipate that regulating the electron−electron correlations will be a powerful tool for engineering the electrical properties in the 2D material systems.

■ ASSOCIATED CONTENT

Supporting Information

Supplementary characterizations, analysis of the hydric TiS_2 nanosheets, demonstration of the transferrable feature and mechanical endurance of the TiS_2 thin film, and experimental details. This material is available free of charge via the Internet at http://pubs.acs.org.

■ AUTHOR INFORMATION

Corresponding Author

czwu@ustc.edu.cn; yxie@ustc.edu.cn

Author Contributions

[§]These authors contributed equally.

Notes

The authors declare no competing financial interest.

■ ACKNOWLEDGMENTS

This work was financially supported by the National Basic Research Program of China (no. 2009CB939901), National Natural Science Foundation of China (nos. 21222101, 11074229, 11132009, 11079004, J1030412), Chinese Academy of Science (XDB01020300), Program for New Century

Excellent Talents in University, and the Fundamental Research Funds for the Central Universities (nos. WK2340000035 and WK2310000024).

REFERENCES

(1) Pushparaj, V. L.; Shaijumon, M. M.; Kumar, A.; Murugesan, S.; Ci, L.; Vajtai, R.; Linhardt, R. J.; Nalamasu, O.; Ajayan, P. M. *Proc. Natl. Acad. Sci. U.S.A.* **2007**, *104*, 13574.
(2) Service, R. F. *Science* **2009**, *324*, 875.
(3) Eda, G.; Fanchini, G.; Chhowalla, M. *Nat. Nanotechnol.* **2008**, *3*, 270.
(4) Li, X.; Zhang, G.; Bai, X.; Sun, X.; Wang, X.; Wang, E.; Dai, H. *Nat. Nanotechnol.* **2008**, *3*, 538.
(5) Feng, J.; Sun, X.; Wu, C.; Peng, L.; Lin, C.; Hu, S.; Yang, J.; Xie, Y. *J. Am. Chem. Soc.* **2011**, *133*, 17832.
(6) Kim, K. S.; Zhao, Y.; Jang, H.; Lee, S. Y.; Kim, J. M.; Kim, K. S.; Ahn, J.-H.; Kim, P.; Choi, J.-Y.; Hong, B. H. *Nature* **2009**, *457*, 706.
(7) Zheng, Q.; Ip, W. H.; Lin, X.; Yousefi, N.; Yeung, K. K.; Li, Z.; Kim, J.-K. *ACS Nano* **2011**, *5*, 6039.
(8) Bae, S.; Kim, H.; Lee, Y.; Xu, X.; Park, J.-S.; Zheng, Y.; Balakrishnan, J.; Lei, T.; Ri Kim, H.; Song, Y. I.; Kim, Y.-J.; Kim, K. S.; Ozyilmaz, B.; Ahn, J.-H.; Hong, B. H.; Iijima, S. *Nat. Nanotechnol.* **2010**, *5*, 574.
(9) Wang, H.; Wang, G.; Bao, P.; Yang, S.; Zhu, W.; Xie, X.; Zhang, W.-J. *J. Am. Chem. Soc.* **2012**, *134*, 3627.
(10) Liu, C.; Yu, Z.; Neff, D.; Zhamu, A.; Jang, B. Z. *Nano Lett.* **2010**, *10*, 4863.
(11) Simon, P.; Gogotsi, Y. *Nat. Mater.* **2008**, *7*, 845.
(12) Stoller, M. D.; Park, S.; Zhu, Y.; An, J.; Ruoff, R. S. *Nano Lett.* **2008**, *8*, 3498.
(13) Zhang, L. L.; Zhao, X.; Stoller, M. D.; Zhu, Y.; Ji, H.; Murali, S.; Wu, Y.; Perales, S.; Clevenger, B.; Ruoff, R. S. *Nano Lett.* **2012**, *12*, 1806.
(14) Yin, Z.; Sun, S.; Salim, T.; Wu, S.; Huang, X.; He, Q.; Lam, Y. M.; Zhang, H. *ACS Nano* **2010**, *4*, 5263−5268.
(15) Wang, X.; Zhi, L.; Mullen, K. *Nano Lett.* **2007**, *8*, 323.
(16) Rao, C. N. R.; Nag, A. *Eur. J. Inorg. Chem.* **2010**, *2010*, 4244.
(17) Nag, A.; Raidongia, K.; Hembram, K. P. S. S.; Datta, R.; Waghmare, U. V.; Rao, C. N. R. *ACS Nano* **2010**, *4*, 1539.
(18) Feng, J.; Peng, L.; Wu, C.; Sun, X.; Hu, S.; Lin, C.; Dai, J.; Yang, J.; Xie, Y. *Adv. Mater.* **2012**, *24*, 1969.
(19) Fang, C. M.; de Groot, R. A.; Haas, C. *Phys. Rev. B* **1997**, *56*, 4455.
(20) Zeng, Z.; Yin, Z.; Huang, X.; Li, H.; He, Q.; Lu, G.; Boey, F.; Zhang, H. *Angew. Chem., Int. Ed.* **2011**, *50*, 11093.
(21) Zeng, Z.; Sun, T.; Zhu, J.; Huang, X.; Yin, Z.; Lu, G.; Fan, Z.; Yan, Q.; Hng, H. H.; Zhang, H. *Angew. Chem., Int. Ed.* **2012**, *51*, 9052.
(22) Park, K. H.; Choi, J.; Kim, H. J.; Oh, D.-H.; Ahn, J. R.; Son, S. U. *Small* **2008**, *4*, 945.
(23) Plashnitsa, V. V.; Vietmeyer, F.; Petchsang, N.; Tongying, P.; Kosel, T. H.; Kuno, M. *J. Phys. Chem. Lett.* **2012**, *3*, 1554.
(24) Wu, C.; Feng, F.; Feng, J.; Dai, J.; Peng, L.; Zhao, J.; Yang, J.; Si, C.; Wu, Z.; Xie, Y. *J. Am. Chem. Soc.* **2011**, *133*, 13798.
(25) Lee, J.; Lee, S.; Li, G.; Petruska, M. A.; Paine, D. C.; Sun, S. *J. Am. Chem. Soc.* **2012**, *134*, 13410.
(26) Guilmeau, E.; Breard, Y.; Maignan, A. *App. Phys. Lett.* **2011**, *99*, 052107.
(27) Whittingham, M. S.; Gamble, F. R., Jr *Mater. Res. Bull.* **1975**, *10*, 363.
(28) Eda, G.; Yamaguchi, H.; Voiry, D.; Fujita, T.; Chen, M.; Chhowalla, M. *Nano Lett.* **2011**, *11*, 5111.
(29) Let, A. L.; Mainwaring, D. E.; Rix, C.; Murugaraj, P. *J. Non-Cryst. Solids.* **2008**, *354*, 1801.
(30) Erdem, B.; Hunsicker, R. A.; Simmons, G. W.; Sudol, E. D.; Dimonie, V. L.; El-Aasser, M. S. *Langmuir* **2001**, *17*, 2664.
(31) Cai, H. L.; Wu, X. S.; Gao, J. *Chem. Phys. Lett.* **2009**, *467*, 313.
(32) Bockrath, M.; Markovic, N.; Shepard, A.; Tinkham, M.; Gurevich, L.; Kouwenhoven, L. P.; Wu, M. W.; Sohn, L. L. *Nano Lett.* **2002**, *2*, 187.
(33) Zhou, Y.; Freitag, M.; Hone, J.; Staii, C.; Johnson, J. A. T.; Pinto, N. J.; MacDiarmid, A. G. *App. Phys. Lett.* **2003**, *83*, 3800.
(34) Staii, C.; Johnson, A. T.; Pinto, N. J. *Nano Lett.* **2004**, *4*, 859.
(35) Datta, S. S.; Strachan, D. R.; Mele, E. J.; Johnson, A. T. C. *Nano Lett.* **2008**, *9*, 7.
(36) Nickel, J. *HPL-95-60*; Hewlett Packard: Palo Alto, CA, 1995.
(37) Zhou, Y.; Hu, L.; Gruner, G. *App. Phys. Lett.* **2006**, *88*, 123109.